Palaeogeography, Palaeoclimatology, Palaeoecology 637 (2024) 112012

Contents lists available at ScienceDirect

Palaeogeography, Palaeoclimatology, Palaeoecology

journal homepage: www.elsevier.com/locate/palaeo

Palaeoenvironmental changes in the Late Triassic lacustrine facies of the Ordos Basin of Northwest China were driven by multistage volcanic activity: Implications for the understanding the Carnian Pluvial Event

Miruo Lin [a], Kelai Xi [a,*], Yingchang Cao [a,*], Xiaobing Niu [b], Weijiao Ma [a], Xiujuan Wang [b], Shang Xu [a]

[a] Key Laboratory of Deep Oil and Gas, China University of Petroleum (East China), Qingdao 266580, China
[b] PetroChina Changqing Oilfield Company, Xi'an 700018, China

ARTICLE INFO

Editor name: Dr. Howard Falcon-Lang

Keywords:
Carnian age
Environmental change
Volcanic activity
Mercury geochemistry
Carbon isotopic excursion
North China Plate

ABSTRACT

The Carnian Pluvial Event (CPE) induced an intense carbon-cycle disturbance and biological crisis at a global scale. The eruption of the Wrangellia Large Igneous Province (W-LIP) is considered a possible triggering mechanism; however, this cannot fully explain the significant differences in environmental perturbations across different regions. In this paper, we present detailed records of petrography, mercury geochemistry, carbon and sulfur isotopes, trace elements, and provenance data for the Triassic lacustrine facies of the Ordos Basin in the North China Plate, which provide insights into the important effects of volcanic activities, other than the W-LIP, on palaeoenvironment during the CPE interval. Massive emissions of SO_2, CO_2, and pyroclastic deposits resulting from these volcanic activities triggered four humid episodes, each characterized by lake-level rise, negative $\delta^{13}C_{org}$ excursion, a transition from mudstones to organic-rich shales facies, as well as algal bloom within a time span of 180 kyrs. The establishment of an age framework in the Ordos Basin enables comparative analyses of environmental evolution during the Carnian age across the North China Plate, the western Tethys domain, and the South China Plate. During the period of global climate perturbation driven by the W-LIP eruption, we conclude that short-term localized volcanic activities may have further induced high frequentcy environmental perturbations, which influenced biological shifts and increase organic carbon burial. These short-term volcanic activities with different occurrence times and frequencies complicate local-scale palaeoenvironmental evolutions, which may be an important reason contributing to significant differences in environmental perturbations during the CPE interval across different regions of the globe.

1. Introduction

As most attention has focused on global climate changes during the Permian-Triassic boundary (PTB) and end-Triassic intervals, the Triassic climate has been a relatively neglected topic and conventionally considered a stable "hot-house" world characterized by a gradual, monotonous, long-term cooling trend (Preto et al., 2010; Kiessling, 2010). However, as the research further develops, $\delta^{18}O$ of conodont suggests three major temperature perturbations (temperature rises) occurring in the Triassic (Trotter et al., 2015), indicating that the Triassic environmental evolution was actually unstable. Within these intense warming episodes, the climate perturbation during the Carnian age, known as the Carnian Pluvial Event (CPE), lasted for approximately 1 Ma, causing a far-reaching effect on the sedimentary environment and biodiversity (Mueller et al., 2016; Li et al., 2020; Dal Corso et al., 2020; Colombi et al., 2021). During this period, climate changes, including temperature rises, a transition from aridness to extreme humidity, and disturbances in carbon isotopes, have been documented in different parts of the globe (Preto et al., 2010; Dal Corso et al., 2018; Sun et al., 2019). The increase in temperature and rainfall enhanced weathering across Pangaea (Hornung et al., 2007). Increased siliciclastic influx interrupted the growth of carbonate platforms and established anoxic conditions in marine sequences, and then about 33% of marine genera at the Julian–Tuvalian boundary were extinct (Dal Corso et al., 2020). In terrestrial sequences, the occurrence of extremely humid climate induced a transition from evaporitic playa-lake deposits to fluvial sandy

* Corresponding authors.
E-mail addresses: xikelai@upc.edu.cn (K. Xi), caoych@upc.edu.cn (Y. Cao).

https://doi.org/10.1016/j.palaeo.2024.112012
Received 28 May 2023; Received in revised form 27 December 2023; Accepted 1 January 2024
Available online 3 January 2024

deposits or mudstones (Simms and Ruffell, 1989; Shukla et al., 2010), followed by the major turnovers of terrestrial tetrapod vertebrates and flora in the Late Carnian (Furin et al., 2006; Bernardi et al., 2018; Dal Corso et al., 2018).

The intense environmental change and biological shift during the Carnian age have attracted the attention of many researchers on their triggering mechanism (Preto et al., 2010). Due to the increase of pCO_2 in the atmosphere (Berner, 1997) and the carbon-isotope disturbance during the Carnian age, volcanism is gradually regarded as a possible triggering mechanism for the palaeoenvironmental perturbation (Zhao et al., 2022; Dal Corso et al., 2022). It is believed that the eruption of the Wrangellia large igneous province (W-LIP) released significant amounts of greenhouse gases and isotopically light carbon. This process is thought to have induced global warming, humid climate, and negative carbon isotope excursion (NCIE) during the Carnian age because the age of the W-LIP partly coincides with that of the intense climate

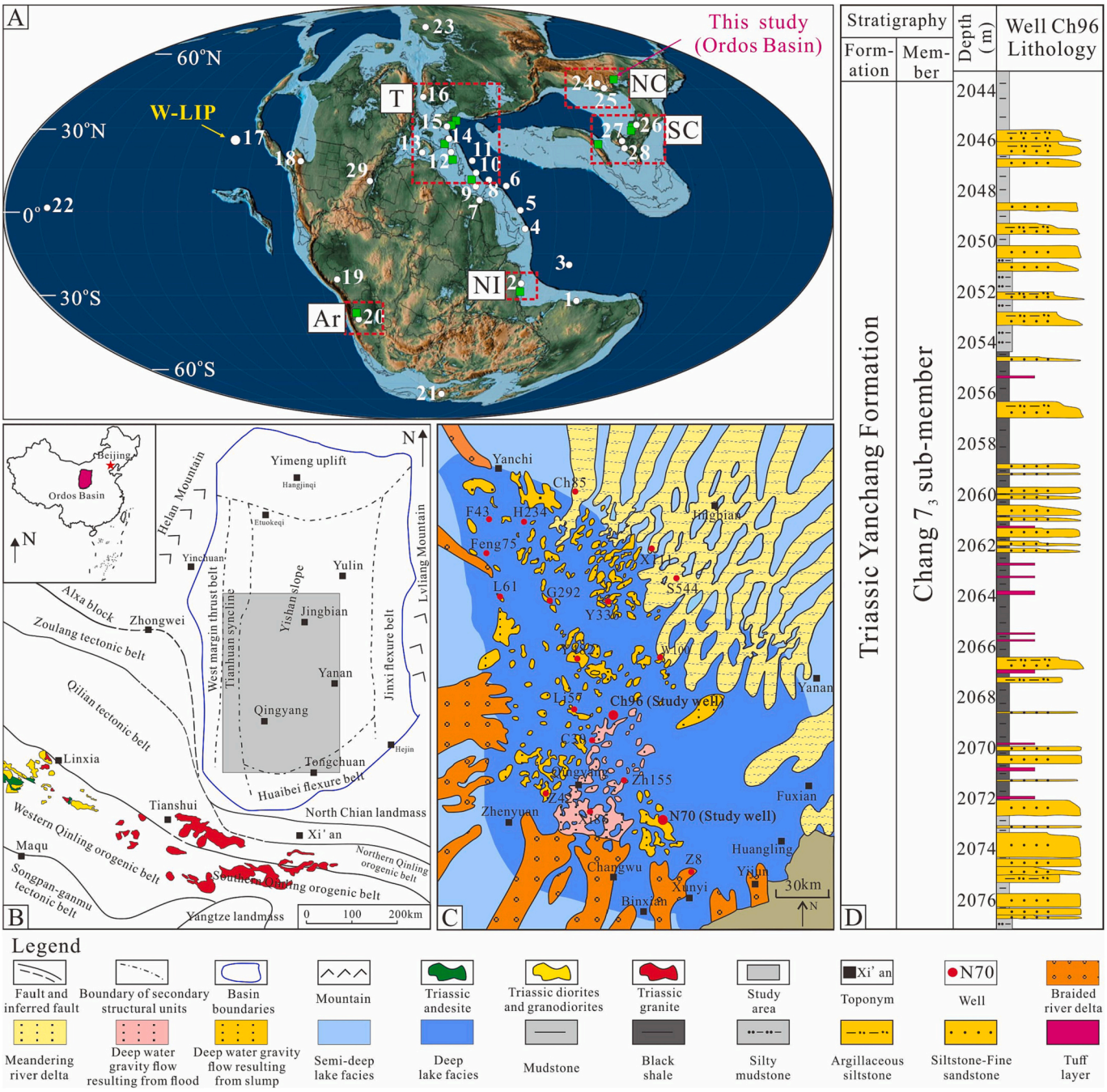

Fig. 1. A, Palaeogeographic map and the volcanic activities during the Carnian age (Late Triassic) (Scotese, 2014). The white dots in A indicate the locations of volcanic activities during the Carnian age. The periods of volcanic activities and the lithology of volcanic rocks are listed in Table S2. Green squares indicate the locations of the recorded environmental perturbation during the Carnian age in five selected regions. B, tectonic location of the Ordos Basin showing distribution of tectonic uplifts, flexure belts and orogenic belts (Zhou et al., 1995). Based on the zircon U—Pb dating, the ages of the granite in the southern Qinling orogenic belt range from 227.3 ± 3.6 to 232 ± 3 Ma (Jiang et al., 2010; Qin et al., 2013). The ages of andesite in the western Qinling orogenic belt are from 226.3 ± 1.1 Ma to 231.7 ± 2.1 Ma (Li et al., 2019); C, planar distribution characteristics of sedimentary facies and well sites in the Chang 7_3 sub-member; D, stratigraphic development characteristics in the Chang 7_3 sub-member. Ar = Argentina, NI = Northeastern India margin, T = western Tethys domain, SC = South China Plate, NC = North China Plate. (For interpretation of the references to colour in this figure legend, the reader is referred to the web version of this article.)

perturbation (Furin et al., 2006; Sun et al., 2016; Ruffell et al., 2016; Dal Corso et al., 2018; Colombi et al., 2021). However, the significant differences in the environmental perturbation and carbon-cycle disturbance among different regions, such as the western Tethys domain and the South China Plate, are still difficult to explain (Sun et al., 2016; Shi et al., 2019). The Carnian age was a time of frequent volcanic activities worldwide. Apart from the W-LIP, many other volcanic centers remained active (Fig. 1A). Current studies primarily focus on the control of the W-LIP eruption on global climate change but neglect the influence of short-term localized volcanic activities on the environmental perturbations. In the Ischigualasto-Villa Unión Basin from Argentina (Ar area in Fig. 1A), the localized volcanic eruption resulted in a 4-m-thick tuff layer within the Ischigualasto Formation during the Carnian age (Colombi et al., 2017, 2021). After the deposition of the tuff layer (228.91 ± 0.14 Ma), the humidity increased significantly, and the dominant sediment changed from floodplain deposits to fluvial deposits. The faunal shifts also coincided with the environmental crisis, including the extinction of the most abundant faunal component, the disappearance of all therapsids, and a complete absence of dinosaurs (Colombi et al., 2021). Similarly, in the northeastern India margin (NI area in Fig. 1A), the intra-plate volcanic eruption (229 ± 2 Ma) along the northeastern Indian margin significantly influenced the sedimentary evolution. The influence was evident in the sudden increase of pyroclastic deposits in sediments and the transition from carbonate rocks to siliciclastic rocks (Meng et al., 2021). These significant changes in sedimentary response and biodiversity indicate that the short-term localized volcanic activities can also significantly affect environmental perturbations during the Carnian age.

The identification of climate changes during the Carnian age is mainly focused on marine sequences but rarely on terrestrial sequences (Sun et al., 2020; Lu et al., 2021). In comparison with marine sequences, terrestrial sequences are more sensitive to environmental evolution. This sensitivity contributes to studying the triggering mechanism of high-resolution paleoenvironment perturbations (Stanley, 1983; Martín-Puertas et al., 2011). In recent years, the disturbance of environmental evolution during the CPE interval has been gradually identified in lacustrine settings, such as the Ordos Basin and Junggar Basin located in the North China Plate (Sun et al., 2020; Zhang et al., 2021a; Peng et al., 2022; Chen et al., 2023). However, after the researchers corresponded the periods of environmental changes and vegetation shifts to the CPE interval, they generally believed that these environmental perturbations and biotic turnovers were caused by the CPE (Sun et al., 2020; Zhang et al., 2021b; Peng et al., 2022). Given that the frequent localized volcanic activities occurred worldwide during the Carnian age, particularly intense volcanic activities in the Qingling orogenic belts from the North China Plate (Jiang et al., 2010; Liu et al., 2018), it remains unclear whether the localized volcanic activities significantly influenced the environmental evolution of their adjacent lake basins.

In this study, we aim to identify sedimentary changes and environmental perturbations during the Carnian age in the Chang 7_3 submember of the Ordos Basin (lacustrine basin). We employ mercury, sulfur, and carbon isotopes and provenance analyses to clarify the causal links between the palaeoenvironmental perturbations and the localized volcanic activities. Finally, the significant role that the localized volcanic activities played in the environmental perturbations during the Carnian age is discussed. The research results may have a significant effect on illuminating the mechanisms of environmental perturbations and carbon-cycle disturbance during the CPE interval.

2. Geological background

The Ordos Basin, located in the western part of the North China Plate (NC area in Fig. 1A), is a large multi-cycle cratonic basin. It is bounded by the Lvliang mountain and Lishi fault to the east, Helan mountain to the west, Xing'an Mongolian orogenic belt and Dengkou-tuoketuo fault to the north, and Qinling orogenic belt and Huaibei flexure belt to the south (Fig. 1B). The collision between the North China Plate and the South China Plate resulted in the formation of the Qinling-Dabie Orogenic Belt in the Late Triassic (Lu et al., 2021), which led to extensive volcanism near the Ordos Basin (white number 24 to 25 in Fig. 1A). Late Triassic intermediate-acidic and intermediate-basic volcanic rocks can be identified near the craters in the southern and western Qinling orogenic belts, respectively (Fig. 1B).

During the sedimentation of the Triassic Yanchang Formation, a large-scale inland depression lake basin was formed as a result of the Indosinian orogeny (Fu et al., 2020). The Yanchang Formation consists of a series of terrigenous clastic rocks primarily of fluvial-lacustrine facies, which are divided into 10 members known as Chang 1–10 (Fu et al., 2020). The Chang 7 member was deposited during the maximum transgression period and received abundant sediments from Archaean–Paleozoic parent rocks in the northeast and southwest provenances (Wang et al., 2013). The Chang 7 member can be further divided into three sub-members: Chang 7_1, Chang 7_2, and Chang 7_3. An extremely warm and humid paleoenvironment was identified during the sedimentary period of the Chang 7_3 sub-member (Fu et al., 2020). The lake level reached the highest during this period compared to other members of the Yanchang Formation. According to the lithological description, sandstones of gravity flow origin (Liu et al., 2021) and massive mudstones mainly occur at the top and bottom of the Chang 7_3 sub-member, while thickly-bedded shales interbedded with multiple tuff layers are steadily deposited between them (Fig. 1C, D). The presence of thickly-bedded lacustrine shales with no sedimentary discontinuities in the Ordos Basin is conducive to reconstructing high-resolution environmental evolution during the Carnian age (Zhang et al., 2016). The sudden occurrence of sedimentary changes in the Ordos Basin, along with nearby volcanism during the Carnian age, provided the favorable conditions for studying the relationship between the environmental perturbations and the localized volcanic activities.

3. Materials and methods

In this section, we provide a brief description of our analytical items and experimental methods. The detailed experimental methods can be found in Supplementary Information S4. For this research, three key core holes with continuous coring (Well N70, C30 and Ch96) in the Chang 7_3 sub-member from the Ordos Basin were selected. Hand-held X-ray fluorescence (ED-XRF) was used to perform nondestructive analysis on the variation of element contents, allowing us to establish the palaeoenvironmental evolution. The bulk mudstones are ground into ~200 mesh powder for X-ray diffraction (XRD) and X-ray fluorescence (XRF) analysis to determine the overall characteristics of mineral composition and element content in the rock samples. Through core observation and microscopic analyses under a Zeiss microscope (Imaging-2 M), the lithofacies and their associations in the Chang 7_3 submember can be classified. Laminated shales were made into thin sections with a thickness of 100 μm. Trace element contents were then obtained using laser ablation inductively coupled plasma mass spectrometry (LA-ICP-MS) in the Guiyang Institute of Geochemistry, Chinese Academy of Sciences. The element contents were calibrated using multiple reference materials (NIST SRM 610, NIST SRM 612, BCR-2G, BIR-1G and BHVO-2G) without applying internal standardization. The inactive element ratios and the REE patterns were used to analyze the provenance of the sediments.

In-situ sulfur isotope analysis of framboidal pyrites was performed by LA- (multi-collector) -ICP-MS (LA-MC-ICP-MS) at the State Key Laboratory of Continental Dynamics, Northwest University, in order to determine the disturbance of sulfur reservoir. IAEA-S-1 (Ag_2S, $\delta^{34}S_{V\text{-}CDT}$ is known to be −0.3‰) was used as standard. S isotopic composition is expressed as a relative value (eqs. S1–S3 in Supplementary Information).

Mercury geochemical analysis was used as a proxy for the intensity of volcanism during the Carnian age. Rock samples were crushed into ~200-mesh powder, and a mercury geochemical analysis was conducted

in the Guiyang Institute of Geochemistry, Chinese Academy of Sciences. Hg concentration was analyzed using CVAFS (Tekran 2500, Tekran® Instruments Corporation, CA). Quantification of Hg was accomplished using a CVAFS analyzer. Hg isotopic composition was determined using a NEPTUNE PLUS MC-ICP-MS. Hg isotopic variations are reported as δ in ‰ referenced to the NIST SRM 3133 Hg standard (analyzed before and after each rock sample) using the eq. S4-S5 in Supplementary Information.

Around 50 g of rock samples were crushed into particles smaller than 0.5 mm in diameter, and spores and pollens were separated at Nanjing Institute of Geology and Palaeontology, Chinese Academy of Sciences. Fluorescence and scanning electron microscope (SEM) observations were performed to identify the algal types in the shales.

$\delta^{13}C_{org}$ of organic matter was conducted to identify if the carbon isotopic disturbance occurred in the Ordos Basin during the Carnian age. A gas chromatography–mass spectrometry (GC–MS) analysis was then used to determine the types of organic matter, followed by biomarker identification. The bulk samples were ground into powders, and some of the powders were used for hydrocarbon extraction and the GC–MS analysis. The GC–MS analysis was performed using Agilent 5977B GC/MSD at the Guangzhou Institute of Geochemistry, Chinese Academy of Sciences. For $\delta^{13}C_{org}$ analysis, the remaining powders were acid-washed with 10% HCl, neutralized with deionized water, weighed into tin capsules, and wrapped. A $\delta^{13}C_{org}$ measurement was carried out using ThermoFinigan Delta Plus XL in the Guiyang Institute of Geochemistry, Chinese Academy of Sciences.

4. Results

4.1. Petrological characteristics of the Chang 7_3 sub-member in the Ordos Basin

4.1.1. Lithofacies characteristics of the Chang 7_3 sub-member

The Chang 7_3 sub-member in the Ordos Basin is characterized by thickly-bedded mudstones interbedded with thin-bedded sandstones. Through core and thin-section observations, we discovered that laminar and massive structures had been developed in the fine-grained sedimentary rocks of the Chang 7_3 sub-member. On this basis, the XRD analysis revealed significant differences in the mineral contents of fine-grained sedimentary rocks, particularly in the contents of quartz, feldspar, pyrite and kaolinite (Fig. 2). Further analyses of rock composition and sedimentary structure revealed four typical lithofacies in the Chang 7_3 sub-member (Fig. 2).

4.1.1.1. Lithofacies 1. Quartz, feldspar, and pyrite are dominant in lithofacies 1 of the laminar structure. The quartz and feldspar contents are in the ranges of 18.3%–37.5% and 7.4%–17.9%, respectively. The pyrite is commonly produced as framboids (Fig. S1A), and its content is up to 45%. Mixed layers of smectite/illite and illite are the two main types of clay minerals. Chlorite is a minor clay mineral a content between 0.5% and 1%. The kaolinite content is too low to be identified by the XRD analysis. Total organic carbon (TOC) in lithofacies 1 ranges from 12.1% to 27.6%. Two types of laminae, including organic-rich lamina (ORL) and silt-grained felsic lamina (SSFL), are generally present in lithofacies 1 (Fig. 2). K-feldspar is predominant in the SSFL, with a content of up to 70% (Xi et al., 2020). The quartz and plagioclase contents are approximately 7.24% and 5.53%, respectively. Grains with

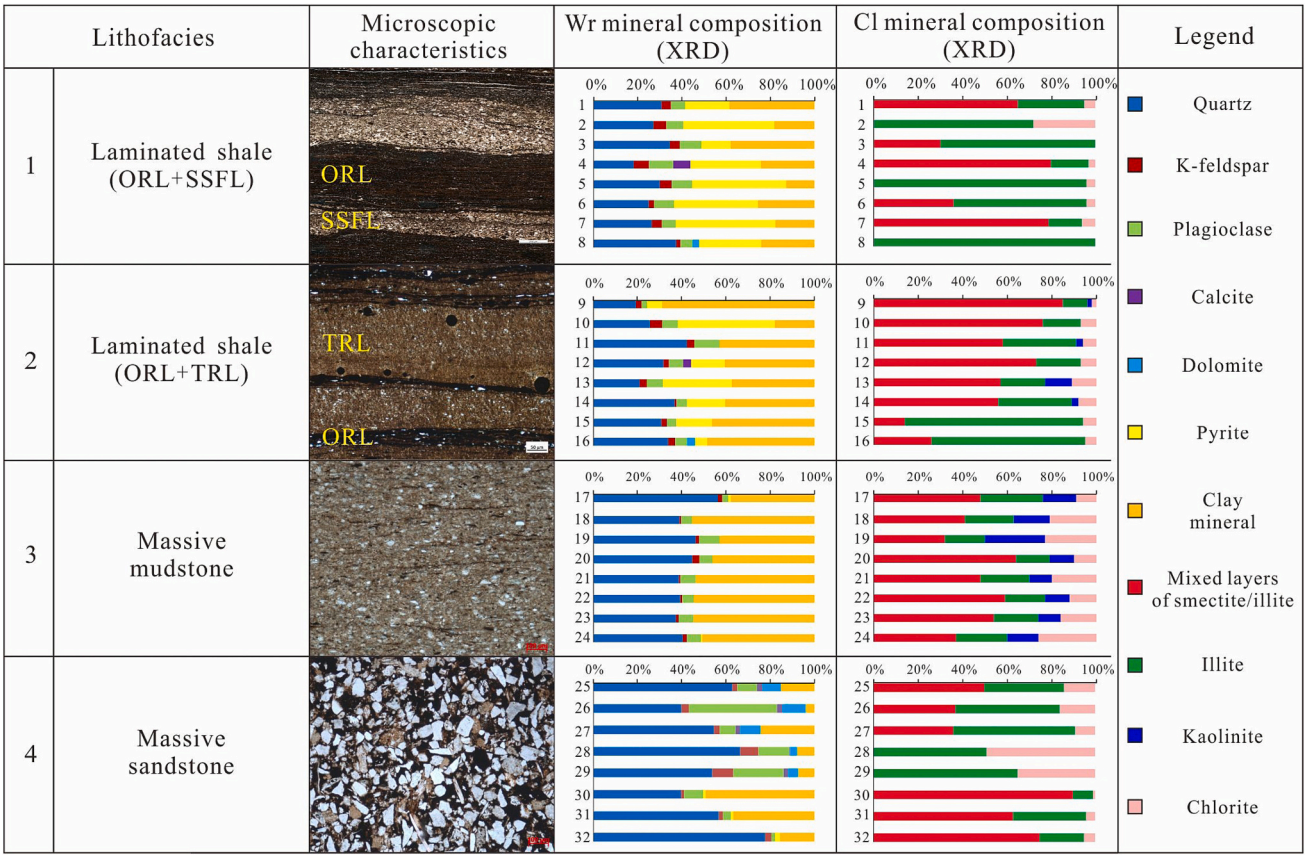

Fig. 2. Petrological characteristics of different lithofacies in the Chang 7_3 sub-member. Wr mineral composition (XRD) indicates the whole rock mineral composition; Cl mineral composition (XRD) indicates the clay mineral composition (XRD). SSFL = silt-grained felsic lamina; ORL = organic-rich lamina; TRL = tuff-rich lamina. 1–32 indicate the sample number.

sharp angles are common in the SSFL. The ORL is composed mainly of mixed layers of smectite/illite, organic matter, and pyrite with contents of up to 52%, 12%, and 9%, respectively (Xi et al., 2020). Minor silt-grained feldspars with sharp angles are also present in ORL.

4.1.1.2. Lithofacies 2. Clay minerals, quartz, and feldspar are dominant in lithofacies 2 of the laminar structure (Fig. 2). The quartz and feldspar contents are 15.3%–28.0% and 4.1%–9.5%, respectively. The clay mineral content is up to 55%. Clay minerals are predominantly mixed layers of smectite/illite and illite, along with minor chlorite (Fig. 2). In terms of the organic content, the TOC in lithofacies 2 ranges from 13.0% to 33.1%. Framboidal pyrite is also common, and its content is mainly distributed from 6.8% to 17.1% (Fig. 2, S1B). The ORL interbedded with tuff-rich lamina (TRL) is a prominent feature lithofacies 2. Mixed layers of smectite/illite with a content up to 80% are the dominant mineral in the TRL (Xi et al., 2020). The contents of organic matter and pyrite are lower in the TRL than in the ORL (Xi et al., 2020).

4.1.1.3. Lithofacies 3. Lithofacies 3, characterized by a massive structure, is predominantly composed of clay minerals with minor pyrite (Fig. 2). The quartz and feldspar contents in lithofacies 3 are 39.9%–47.4% and 4.8%–11.4%, respectively, and are higher than those in lithofacies 1 and 2. Mixed layers of smectite/illite and illite are common in lithofacies 3. Additionally, the kaolinite and chlorite contents are obviously higher than those in lithofacies 1 and 2. TOC in lithofacies 3, ranging from 1.3% to 5.8%, is obviously less than that in the first two lithofacies.

4.1.1.4. Lithofacies 4. Lithofacies 4 is thin (<0.5 m) in the Chang 7_3 sub-member. It is composed of abundant quartz and feldspar mixed with a small amount of clay minerals (Fig. 2).

4.1.2. Sedimentary changes during the Carnian age

The Chang 7_3 sub-member contains two laminated shales (lithofacies 1 and 2), one massive mudstone (lithofacies 3) and one sandstone (lithofacies 4). It is further divided into lower, middle, and upper parts based on the lithofacies associations (Fig. 3). In the lower part, lithofacies 3 and 4 alternately deposited, with rare tuff layers. Gravity-flow-derived sandstones are well developed and account for 70% of the total thickness of the lower part (Fig. 3). In the middle part of the Chang 7_3 sub-member, massive mudstones abruptly change into black shales, with the Al/Ti ratio and TOC increasing (Fig. 3). Lithofacies 1 and 2 and several tuff layers are widely present. Lithofacies 4 mainly occurs as thin-bedded interlayers and accounts for 23% of the total thickness in the middle part. As sedimentary changes occur from the lower to middle part, the geochemical characteristics recorded by the fine-grained sediments show synchronous variations. During these sedimentary changes, the Mo/Ti and V/Ti ratios significantly increase, followed by the increase of C value and CaO/MgO × Al_2O_3 (Fig. 3). In addition, multiple NCIEs showing shifts of about −2‰, along with Hg enrichments, occur in the middle part of the Chang 7_3 sub-member (Fig. 3). Based on zircon U—Pb dating data and chronological constraints, the onset of sedimentary change and intense variation of geochemical characteristics is limited at around 233.2 Ma in the Ordos Basin (S1 in the Supplementary Information; Figs. S4, S6). During the transition from the middle to upper part, the black shales are replaced with massive mudstones once

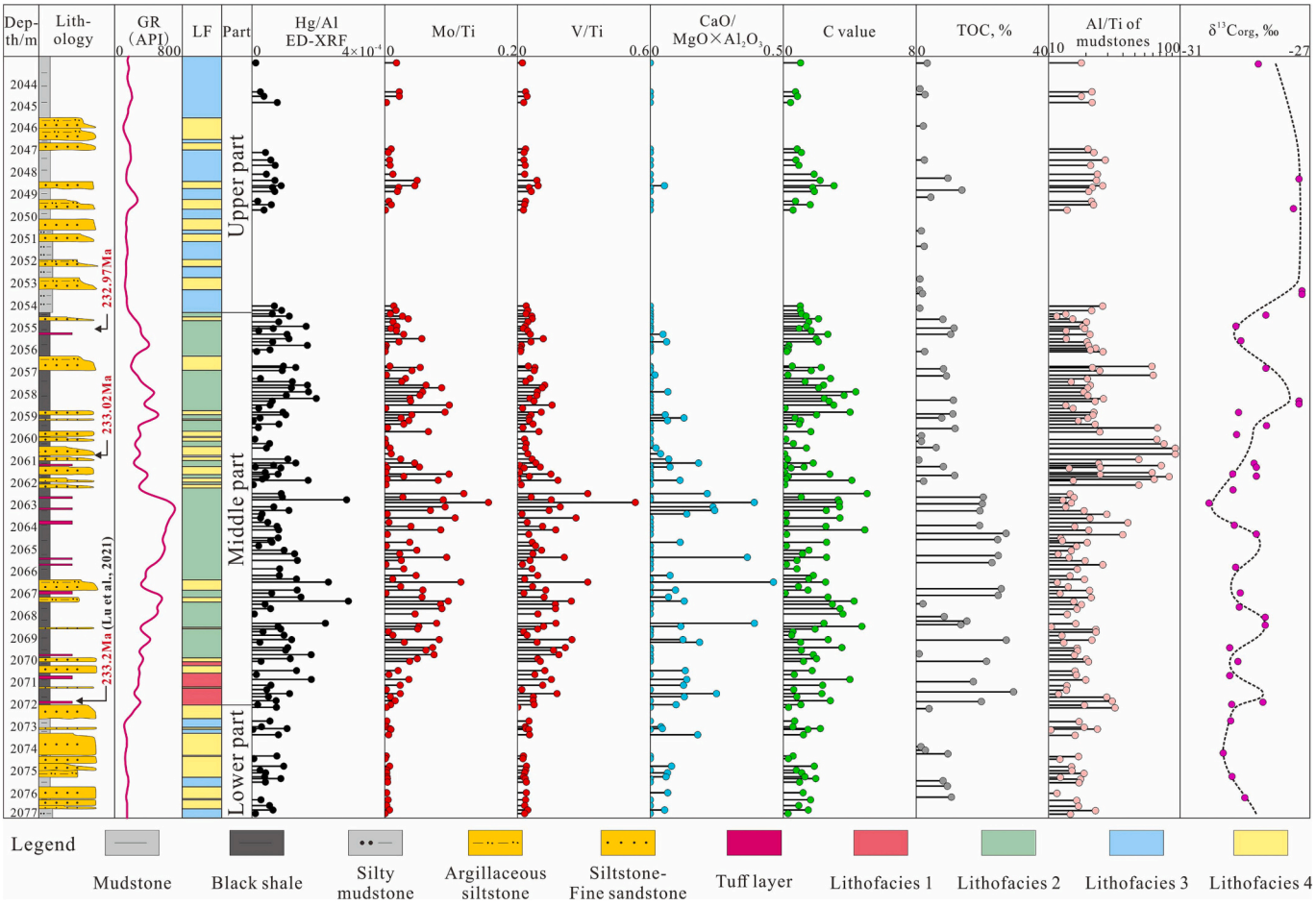

Fig. 3. Sedimentary changes and the variations of geochemical proxies during the Carnian age in the Chang 7_3 sub-member (Well Ch96). LF-lithofacies. C value = Σ (Fe + Mn + Cr + Ni + V + Co)/Σ (Ca + Mg + K + Na + Sr + Ba), where each element in the formula represents the content of the corresponding element.

again, while the tuff layers are barely identified. The thickness of lithofacies 4 gradually increases and accounts for 34% of the total thickness of the upper part. Along with the sedimentary changes, the Mo/Ti and V/Ti ratios suddenly drop, and C value and CaO/MgO × Al_2O_3 decrease, returning to levels similar to those in the lower part (Fig. 3). The Hg/Al ratio also shows a decreasing trend. In this stage, the content of ^{13}C increases obviously, and the NCIE disappears (Fig. 3).

4.2. Mercury, carbon, and sulfur isotope variations

In the Chang 7_3 sub-member, sedimentary changes, intense variations of geochemical parameters and Hg enrichment synchronously occur in the middle part (Fig. 3). Therefore, we conducted a detailed Hg geochemical analysis,focusing on the middle part of the Chang 7_3 sub-member. In particular, Hg isotopes that undergo mass-dependent fractionation (MDF) and mass-independent fractionation (MIF) can be used to trace Hg sources and cycling (Thibodeau et al., 2016). According to the correlation analysis, the correlation between the Hg content and TOC and that between the Hg content and total sulfur content are both poor (Figs. S7A—B), while the Hg content is positively correlated with the aluminum content (Fig. S7C). Therefore, we selected the Hg/Al ratio to trace the levels of increased Hg loading. Four intervals of Hg enrichment, represented by the Hg/Al ratio, can be observed in the middle part (Fig. 4). Notably, the tuff layers only occur within the intervals where the Hg/Al ratio rises abnormally, and the thickness of the tuff layers seems to increase with the Hg/Al ratio (Fig. 4). The MDF expressed by the $\delta^{202}Hg$ value is primarily negative, ranging from −2.27‰ to −1.36‰ (Fig. 5). $\triangle^{199}Hg$ is mainly concentrated around zero (Fig. 5), suggesting no significant MIF. Furthermore, intense carbon (C) and sulfur (S) isotope perturbations can be observed in the four Hg-enriched intervals (Fig. 5). Negative sulfur and carbon isotope excursions occur almost simultaneously, reaching up to −8‰ and −1.5‰, respectively (Fig. 5). Additionally, significant MIF of sulfur isotopes (S-MIF) can be identified, reaching up to around −1‰ (Fig. 5).

5. Discussion

5.1. Triggering mechanism of the environmental perturbation during the Carnian age in the Ordos Basin

During the Carnian age, the transition from massive mudstones to black shales and the increase of Mo/Ti and V/Ti ratios indicate a significant change in the sedimentary environment after 233.2 Ma (Fig. 3) (Brucker et al., 2011; Meng et al., 2021; Zhao et al., 2022). Mo/Ti and V/Ti ratios are common indices to assess the reducibility of the water column; the increase of both ratios indicates the increase of the reducibility, and vice versa (Brucker et al., 2011; Zhang et al., 2017). Therefore, in conjunction with the sedimentary changes, the reducibility of the water column increases obviously (Fig. 3). The C value, which is a chemical index used for paleoclimatic interpretation of clayey sediments, is often utilized to determine the humidity of the environment recorded by lacustrine shales (Qiu et al., 2015). An increase in this index suggests an increase in humidity, while the opposite indicates a decrease (Qiu et al., 2015). Additionally, CaO/MgO × Al_2O_3 has been successfully used for reconstructing the temperature in the Ordos Basin (Fu et al., 2018). An increase in this index indicates an increase in the temperature, while an decrease suggests a decrease in the temperature. Based on these indices, the increased humidity and raised temperature occurred following the sedimentary changes (Fig. 3). Furthermore, hygrophytic palynological assemblages, such as *Caytonipollenites pallidus, Osmundacidites parvus, Chasmatosporites, Pityosporites*, and *Podocarpidites*, have been identified in the middle part, providing support for a significant increase during the deposition of the middle part of the Chang 7_3 sub-member (Fig. S9). The occurrence of the NCIE, increases in CaO/MgO × Al_2O_3 and C value, and the appearance of hygrophytic palynological assemblages (Figs. 3 and S9) demonstrated that multistage humid

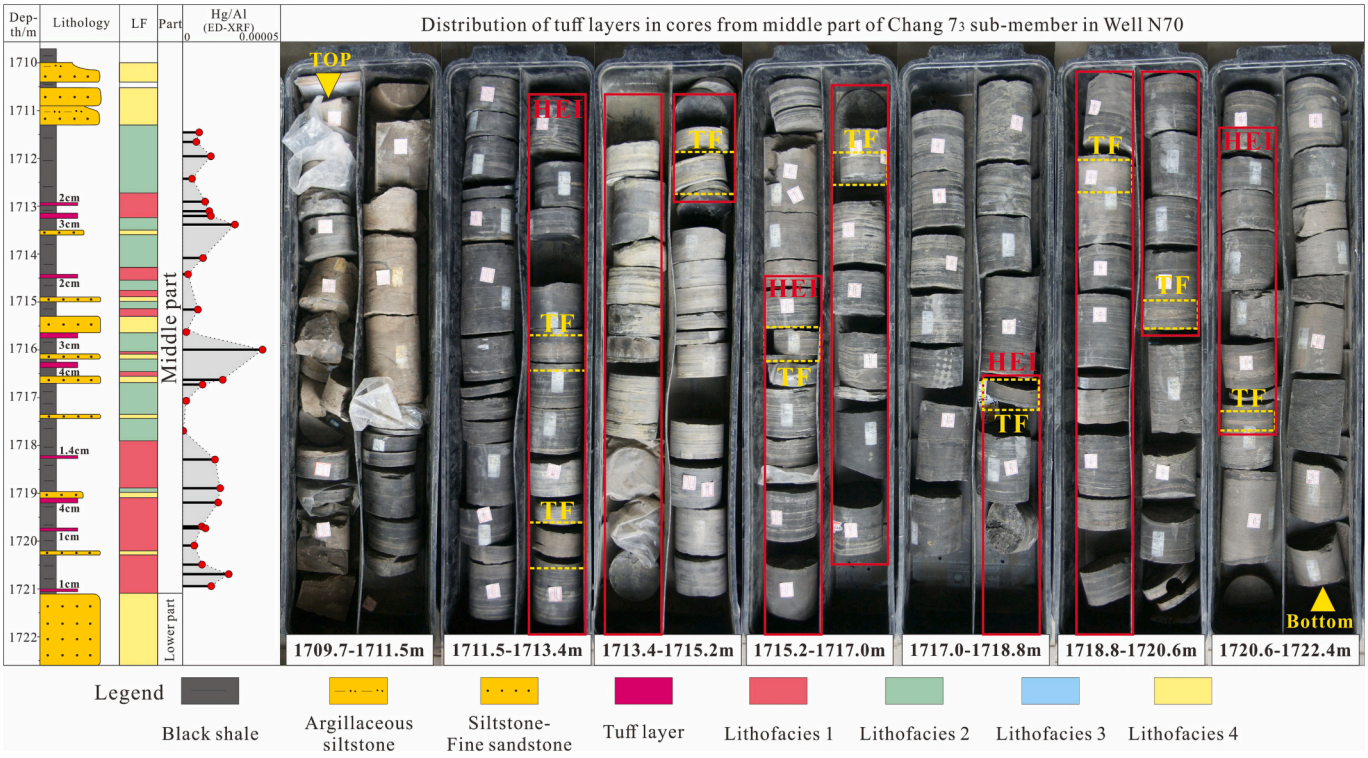

Fig. 4. Distribution of tuff layers in the middle part of Chang 7_3 sub-member in Well N70. The solid red boxes indicate the Hg-enriched intervals, and the yellow dotted boxes indicate the locations of tuff layer deposition. Tuff layers tend to be reddish brown on the core, with a straight top-to-bottom interface (Qiu et al., 2014). Microscopic observation shows that the rod-like feldspars with sharp angles are enriched in the tuff layers (Fig. S8). HEI = Hg-enriched interval; TF = tuff layer. (For interpretation of the references to colour in this figure legend, the reader is referred to the web version of this article.)

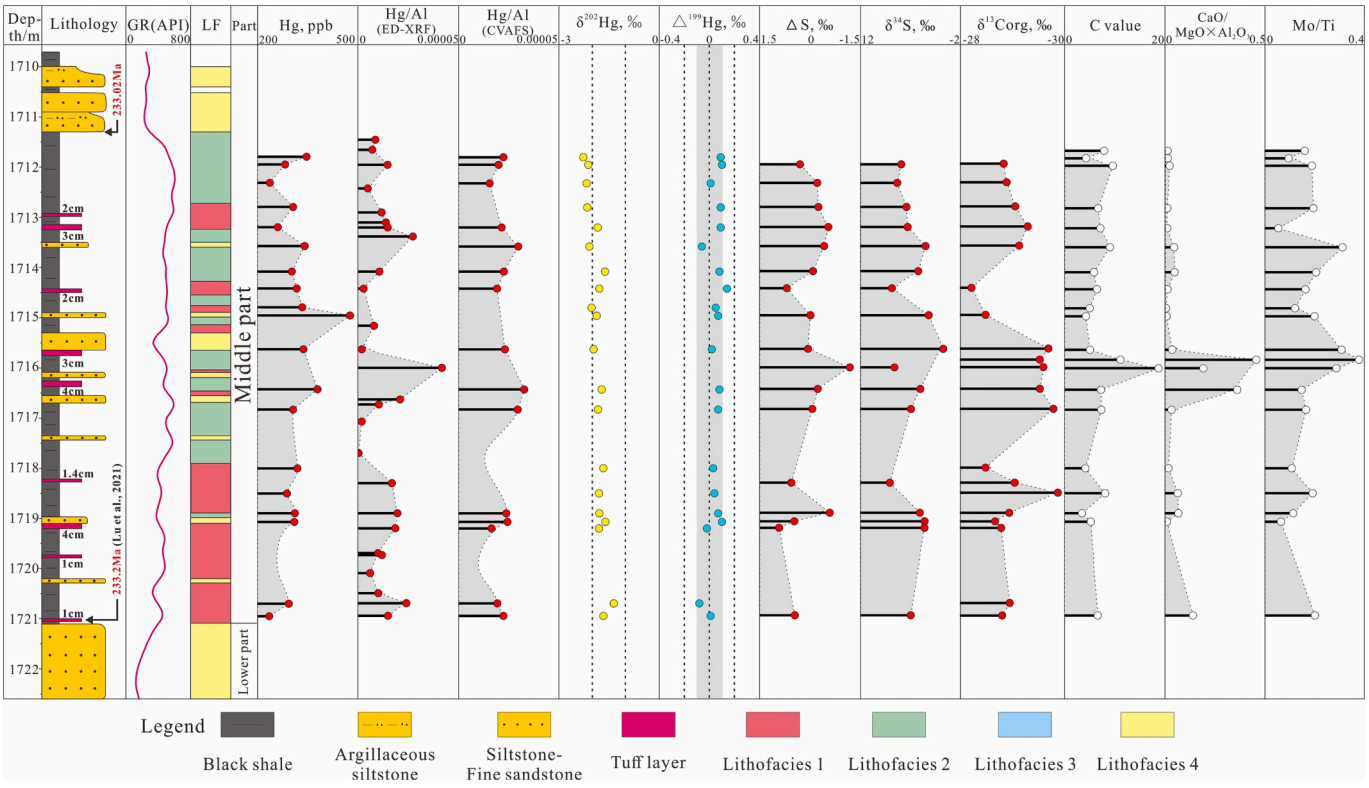

Fig. 5. Mercury geochemistry, carbon and sulfur isotope variations and palaeoenvironmental evolution recorded by thickly-bedded shales in the Chang 7_3 sub-member (Well N70). LF = lithofacies.

episodes and carbon-cycle disturbances synchronously occurred in the Ordos Basin after 233.2 Ma. During this period, Hg was simultaneously enriched (Fig. 3), resulting in the formation of several Hg/Al peaks (Fig. 5). This good matching relationship may serve as a key aspect in studying the triggering mechanisms of the environmental perturbation in the Ordos Basin during the Carnian age.

It is known that volcanism is a substantial source of Hg in geological history (Sanei et al., 2012; Blum et al., 2014). Large volcanic eruptions cause substantial short-term increases in the atmospheric Hg burden (Thibodeau et al., 2016). The residence time of Hg^0 (g) in the atmosphere is approximately 1.5 yr (Meixnerová et al., 2021), so that the Hg^0 can be largely removed through two pathways (Grasby et al., 2017; Them II et al., 2019): (1) transformation to oxidized Hg^{2+} species, and easy deposition through wet/dry deposition; (2) direct uptake by vegetation and soils followed by oxidation. Organic matter, pyrite, and clay minerals further absorb the produced Hg^{2+} species, inducing Hg enrichment in sediments (Percival et al., 2017; Thibodeau et al., 2016). In the Hg-enriched intervals, the negative $\delta^{202}Hg$ values recorded in the middle part of the Chang 7_3 sub-member (Fig. 5) are similar to those of volcanic emissions ($\delta^{202}Hg$ ranged from −3.42‰ to 0.58‰) (Hintelmann and Lu, 2003; Thibodeau et al., 2016). The direct isotopic measurements of volcanic Hg emissions also show no measurable MIF ($\triangle^{199}Hg \approx 0‰$) (Fig. 5) (Zambardi et al., 2009). The significant S-MIF ($\Delta S \approx -1‰$) can be identified synchronously (Fig. 5). There are two main factors causing the negative excursion of $\Delta^{33}S$: (1) at least the Plinian volcanic eruptions occurred. Plinian volcanic eruptions are strong enough to send $SO_{2(g)}$ into the stratosphere, resulting in the photochemical reaction of $SO_{2(g)}$ and the formation of a negative bias of $\triangle^{33}S$ (Ohmoto, 2020). The negative deviation of $\Delta^{33}S$ formed in this process can reach −1‰ (Ohmoto, 2020). However, it is difficult for a small volcanic eruption to send SO_2 into the stratosphere and cause a significant negative shift of $\Delta^{33}S$ (Baroni et al., 2007). (2) The mixing of S-poor shallow water with S-rich deep water results in a negative bias of $\triangle^{33}S$ (Shen et al., 2011). The negative deviation of $\Delta^{33}S$ formed in this process can only reach −0.05‰. Therefore, the significant S-MIF ($\Delta S \approx -1‰$) confirms that at least the Plinian eruptions occurred in the Hg-enriched intervals (Fig. 5) (Ohmoto, 2020). The additional Hg preserved in the middle part of the Chang 7_3 sub-member mainly derives from the intense volcanic activity.

The presence of several Hg/Al peaks recorded in the middle part of the Chang 7_3 sub-member further coincides with multistage disturbances of carbon and sulfur isotopes, as well as palaeoenvironmental perturbation (simultaneous increases in humidity, temperature and reducibility) (Fig. 5). This suggests that the massive releases of CO_2 (g) and SO_2 (g) into atmosphere by each intense volcanic activity pulse influenced the environmental evolution in the Ordos Basin during the Carnian age. Abundant SO_2 aerosols reflect or absorb sunlight, triggering episodes of cooling (Wignall, 2001; Guex et al., 2004). Although this effect lasted only for a few years, making it difficult to identify from geological records (Mchone, 2003), the disturbance in natural sulfur reservoirs caused by the volcanic SO_2 input can be detected (Philippot et al., 2012). The volcanic SO_2 (the $\delta^{34}S$ is approximately 0‰) contains more ^{32}S than the sulfate in lake water (Fike et al., 2015). Therefore, the massive injection of volcanic SO_2 into the lake water induced the negative sulfur isotope excursions (NSIE) of framboidal pyrite in the Hg-enriched intervals (Fig. 5). After the effect of SO_2, the abundant CO_2 in the atmosphere caused the greenhouse effect, lasting for several centuries (Mchone, 2003; Wang et al., 2018). Volcanic CO_2 ($\delta^{13}C \leq -5‰$) contains more isotopically light carbon than the lake water ($\delta^{13}C$ of the lacustrine carbonate rocks ranged from +2.9‰ to +9.3‰, indicating the C isotopic characteristics of dissolved CO_2 in the lake water) (Korte and Kozur, 2010; Xi et al., 2019). The massive and continuous injection of light ^{12}C, therefore, can induce a significant NCIE of organic matter (Korte and Kozur, 2010) (Fig. 5). However, there are several ways to generate the NCIE of $\delta^{13}C_{org}$. The maturities of the organic matter in the Chang 7_3 sub-member are mainly in the stage of low maturity to mature (Xi et al., 2020). The difference in the buried depth of shale samples is <10 m (Fig. 5). These demonstrates that the NCIEs cannot be attributed

to variation in the thermal evolution of organic matter. Therefore, differences in the sources of organic matter and the injection of additional ^{12}C may contribute to a significant negative bias of carbon isotopes (Jin et al., 2021; Zhang et al., 2021a). Both Jin et al. (2021) and Zhang et al. (2021a) have reported that variations in the organic matter types significantly influence organic carbon isotopes in the Chang 7 member. The increases in algae and plankton in lake sediments can result in a decrease in $\delta^{13}C_{org}$ (Meyers, 1994; Andrusevich et al., 1998), while the incorporation of terrigenous organic matter can lead to positive excursion of $\delta^{13}C_{org}$ (Jin et al., 2021; Zhang et al., 2021b). However, the plot of Hydrogen index (HI) and Tmax shows no significant change in the types of organic matter in the black shales of the Chang 7_3 sub-member (Fig. S10). In particular, under similar Tmax conditions, the HI value of the 1716.83 m shale sample is lower than that of the 1720.95 m shale sample, indicating the organic matter type in the 1720.95 m shale sample is more inclined towards Type I compared to the 1716.83 m shale sample. In theory, if the organic matter type primarily controls the carbon isotope, the carbon isotopic value of the 1720.95 m shale sample should be lower than that of the 1716.83 m shale sample (Meyers, 1994; Andrusevich et al., 1998). However, the NCIE in the 1716.83 m shale sample is greater than that in the 1720.95 m shale sample (Fig. 5). Therefore, during the deposition of black shales in the Chang 7_3 sub-member, additional ^{12}C injection should be an important cause of the NCIE. Given that the occurrence of NCIE corresponds to the Hg-enriched intervals, the large amount of volcanic CO_2 injection would be an important factor contributing to the NCIE during the deposition of the Chang 7_3 sub-member. Due to the short-lived effect of SO_2 on temperature, the injection of CO_2 induced an abnormally high greenhouse effect, resulting in increased humidity and temperature in the several Hg-enriched intervals (Fig. 5). The increased rainfall also led to a synchronous lake-level rise, and the increased reducibility of the water column and decreased thickness of SSFL supported this trend (S2 in the Supplementary Information; Fig. S11). Therefore, the greenhouse effects resulting from multistage intense volcanic activities during the Carnian age ultimately triggered the environmental perturbation in the Ordos Basin. Such intense environmental perturbation caused by the volcanic activity during the Carnian age is easily associated with the role of the W-LIP eruption. However, the chronological constraints indicate that at least four humid episodes and four NCIEs occurred within 0.18 Ma in the Ordos Basin located on the North China Plate (Figs. 3, 5, S6). The situations of the western Tethys domain (four humid episodes and four NCIEs occurring within 2.4 Ma) and the South China Plate (one humid episode and one NCIE occurring within 180 kyrs) are significantly different (Dal Corso et al., 2018; Shi et al., 2019). These obvious differences in the environmental perturbation and carbon-cycle disturbance between different parts of the globe seem difficult to explain by the W-LIP eruption alone. One explanation might be differences in sampling density, but further research confirmed that this is controlled by the localized volcanic activities. The reason is that localized volcanic activities may induce local-scale environmental perturbation (Colombi et al., 2021) and carbon-cycle disturbance (Hernández et al., 2001a, 2001b). Taking the change in the carbon isotope as an example, previous studies have shown that in the rock record, there is evidence that the impact of the local-scale carbon cycle on $\delta^{13}C$ is nontrivial (Panchuk et al., 2006). In modern semi-restricted marine environments, due to the large input of ^{12}C at a local scale, the influence of the local carbon cycle on $\delta^{13}C$ can be substantial (Lloyd, 1964; Patterson and Walter, 1994). Therefore, the carbon isotope record may contain much more of a local-scale carbon cycling signal than is generally appreciated (Panchuk et al., 2006). The local-scale differences in carbon cycling finally superimpose on the larger-scale global carbon cycle record (Panchuk et al., 2006). During the continuous localized volcanic activities, a large amount of CO_2 released from the crater accumulated in the area around the crater, affecting the CO_2 concentrations in the area near the crater. This situation was confirmed by actual observations (Hernández et al., 2001a). The researchers found that the soil CO_2 flux increased significantly near the craters (within several kilometers) during the fumarolic activity of volcanos lasting for about one year (Hernández et al., 2001b; Carapezza et al., 2011). The injection of a large amount of volcanic CO_2 also significantly influenced the carbon isotopic value of CO_2 in the soil near the crater (Hernández et al., 2001b). Therefore, it is necessary to consider the impacts of localized volcanic activities on the environmental perturbation and carbon-cycle disturbance.

Volcanic activities occurred in various regions around the world during the Carnian age (Fig. 1A). A key issue is how the environmental perturbation in the Ordos Basin was triggered. In the middle part of the Chang 7_3 sub-member, the presence of tuff layers only in the Hg-enriched intervals suggests the existence of a localized volcanic source (Fig. 4) (Lu et al., 2021). Zircon U—Pb dating of the extrusive rocks (Fig. 1B; #24 and #25 in Table S2) indicates that the ages of volcanic activities in the Qinling orogenic belts coincide with those of Hg enrichment and environmental perturbation in the Ordos Basin (Fig. 3). Similarities in the ratios of inactive elements and rare earth elements (REEs) patterns (Fig. 6A–C) confirm that the tuff layers in the Ordos Basin originated from the volcanic eruptions in the Qinling orogenic belts (Qiu et al., 2014). Therefore, the deposition of tuff layers at the onset of multiple Hg-enriched intervals (Fig. 4) suggests that the volcanic activities in the Qinling orogenic belts are a major factor contributing to Hg enrichment and environmental perturbation in the Ordos Basin during the Carnian age.

Compared to the massive mudstones, the black shales contain more rod-like feldspars (Fig. S12) and show higher Al/Ti ratios (Fig. 3), suggesting that their provenance has changed into pyroclastic deposits (Niem, 1977; Hayashi et al., 1997; Qiu et al., 2014). However, three types of laminae with different mineral compositions can be identified within the black shales (Fig. 2). Considering the possible differences in provenance, the sources of different types of laminae are discussed separately. In-situ geochemical analyses confirm that the sediments in the three types of laminae are no longer sourced from the southwest and northeast provenance areas (Fig. 6D–H). The Zr/TiO_2–Nb/Y plot indicates that the sediments in the TRL and ORL mainly derive from intermediate-basic pyroclastic deposits, while the sediments in the SSFL mainly derive from intermediate-acid pyroclastic deposits (Fig. 6I). Intermediate-acid and intermediate-basic extrusive rocks surrounding the craters are exactly preserved in the southern and western Qinling orogenic belts, respectively (Fig. 1B). Similarities in the ratios of inactive elements and the patterns of REEs confirm that the sediments in the SSFL mainly derive from the pyroclastic deposits produced by the volcanic eruption in the southern Qinling orogenic belt (Fig. 6A–C). The inorganic sediments in the ORL and TRL mainly derive from the pyroclastic deposits produced by the volcanic eruption in the western Qinling orogenic belt (Fig. 6A–C). Therefore, the volcanic activities in the Qinling orogenic belts not only trigger environmental perturbation but also induce the changes in sediment provenance, resulting in sedimentary changes in the Ordos Basin during the Carnian age.

Before the intense volcanic activities in the Qinling orogenic belts, the lake level of the Ordos Basin was relatively low (Fig. 7A). The sediments in mudstones were primarily supplied by the southwest and northeast provenance areas. During the Plinian eruptions in the Qinling orogenic belts, extreme conditions, such as increased temperature and acid rain (due to volcanic SO_2 input), occurred in the Ordos Basin (Fig. 7B). Additionally, the massive injection of pyroclastic deposits altered the sediment provenance and simultaneously promoted the substantial inputs of nutrients (e.g. P, Fe) into the lake (Fig. 7C, S13). The extreme conditions may kill the less heat-tolerant *Chrysophyceae*, while the nutrient inputs stimulate the bloom of heat- and acid-resistant algae, such as *Botryococcus* and *Cyanophyta* (Roijackers and Kessels, 1986; Tasić et al., 2016; Carrillo and Díaz-Villanueva, 2021) (Figs. S13, S14). The massive algae absorbed the CO_2 from the atmosphere through photosynthesis and produced organic carbon during Plinian eruptions. Meanwhile, with increased humidity, the rapid rise of the lake level enhanced reducibility, creating favorable conditions for organic carbon

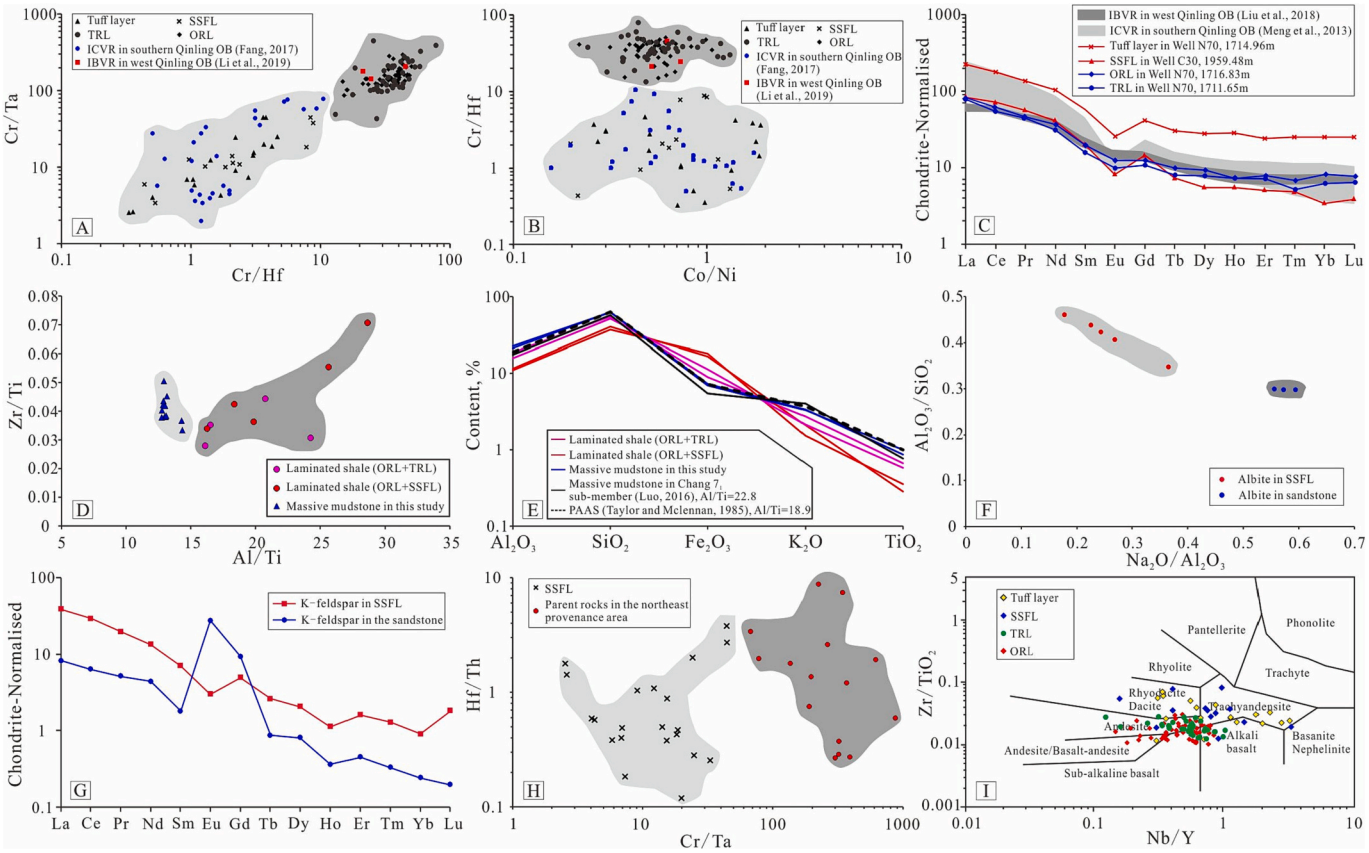

Fig. 6. Geochemical characteristics of lamina, minerals and volcanic rocks. A-B, cross plots showing the ratios of inactive elements of tuff layers, shale laminae and the volcanic rocks in the southern and western Qinling orogenic belts; C, REE patterns of tuff layers, shale laminae and the volcanic rocks from the southern and western Qinling orogenic belts; D, cross plot of the inactive element ratios in laminated shales and massive mudstones; E, major element patterns of massive mudstones and laminated shales; F, cross plot of the element ratios in the albite particles in SSFL and sandstones; G, REE patterns of the K-feldspar particles in SSFL and sandstones; H, cross plot of the inactive element ratios in SSFL and the parent rocks from the northeast provenance area; I, Zr/TiO_2-Nb/Y plot showing the provenance of different lamina and tuff layers; ICVR = intermediate-acidic volcanic rocks; IBVR = intermediate-basic volcanic rocks; OB = orogenic belts; SSFL = silt-grained felsic lamina; ORL = organic-rich lamina; TRL = tuff-rich lamina. Sandstones in C and D are sourced from the parent rocks in the southwest provenance areas.

preservation and ultimately resulting in the black-shale deposition (Figs. 5, 7C). After the intense volcanic activities in the Qinling orogenic belts, the humid environmental perturbation gradually ceased, and the lake level fell (Fig. 7D). Reduced reducibility of the water column and decreased nutrient inputs eventually resulted in the transition from black shales to massive mudstones (Fig. 7D).

5.2. *Significance role that localized volcanic activities played in the environmental perturbations during the Carnian age*

The causal link between the environmental perturbations in the Ordos Basin and localized volcanism highlights the significant role of localized volcanic activities during the Carnian age. During the period of global climate perturbation controlled by the W-LIP eruption (CPE interval), volcanic activities occurred worldwide with different occurrence times and frequencies (Fig. 1A; Table S2), which likely influenced the environmental evolution in various regions. Previous researchers indicated that at least four short-lived negative $\delta^{13}C_{org}$ excursions occurred in the western Tethys domain after 234 Ma, while only one long-lasting negative $\delta^{13}C_{org}$ excursion occurred in the South China Plate (Fig. 8) (Sun et al., 2016, 2019; Li et al., 2020). Alternate occurrence of the siliciclastic sediments and metazoan carbonate platform, along with frequent temperature fluctuations, can be identified after 234 Ma in the western Tethys domain (Fig. 8A); the stable siliciclastic deposition without frequent temperature fluctuations can be identified in the South China Plate (Fig. 8B). The reason for the above significant differences between the western Tethys domain and the South China Plate during the same period is unclear (Sun et al., 2016; Shi et al., 2019). The characteristics of Hg anomalies confirm that different volcanic processes were recorded in these two regions because the additional mercury in their sediments mainly came from volcanism (Fig. 8) (Mazaheri-Johari et al., 2021; Zhao et al., 2022). The difference of NCIEs in the two regions also suggests different processes of carbon-cycle disturbance (Fig. 8). Obviously, these significant differences are difficult to explain using the W-LIP alone. Previous researchers also used the volume of basalts to calculate that the light carbon released by the W-LIP eruption was insufficient to cause such a large disturbance in the carbon cycle during the CPE interval worldwide (Sun et al., 2019; Li et al., 2020). Therefore, additional light carbon needs to be injected in different regions to cause the NCIE to the present value. In our study, we took the Ordos Basin as an example and confirmed that the localized volcanic activities could release sufficient CO_2 to induce increases in the local-scale temperature and humidity and the NCIE during the CPE interval. The local-scale differences in carbon cycling were then superimposed on the larger-scale global carbon cycle record (Panchuk et al., 2006). Therefore, the light carbon released by the localized volcanic activities may effectively supplement the amount of light carbon required in different regions, leading to the local-scale carbon-cycle disturbance being superimposed global carbon-cycle disturbance. We investigated and found that many volcanic activities occurred in both the western Tethys domain and the South China Plate during the CPE interval in the Triassic Carnian age (The white circles in T and SC areas

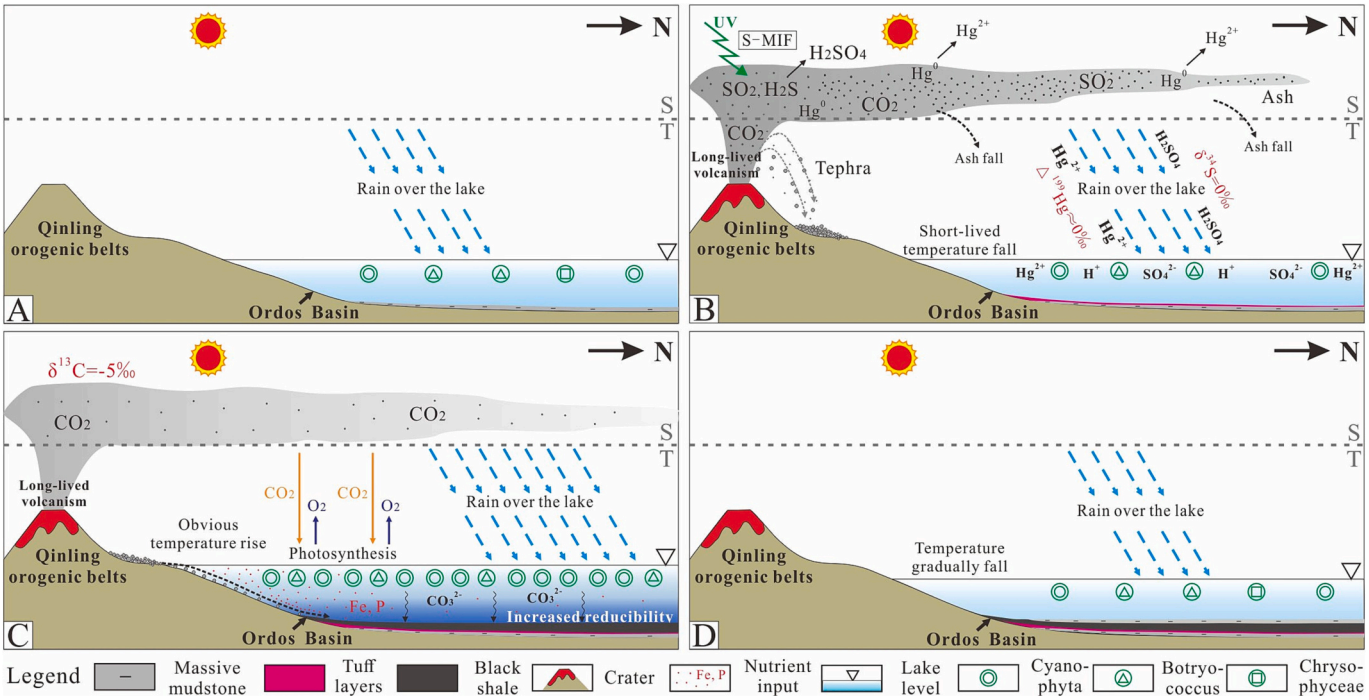

Fig. 7. Formation modal of the environmental perturbation in the Ordos Basin under the constraint of the volcanism in the Qinling orogenic belts during the Carnian age. A, deposition of massive mudstone before the onset of volcanism in the Qinling orogenic belts. B, the short-lived subsidence processes of the sulfides and mercury of volcanic origin during the period of volcanism in the Qinling orogenic belts. C, long-termed accumulation of CO_2 resulted in the greenhouse effect, triggering the environmental perturbation in the Ordos Basin. Long-lived volcanism resulted in the large concentration of CO_2 around the Qinling orogenic belts, which induced the greenhouse effect in the areas of high CO_2 abundance, leading to the increase of temperature and rainfall, as well as lake level rise, in the Ordos Basin. Meanwhile, the pyroclastic deposits in the Qinling orogenic belts entered the Ordos Basin to provide the source for black shales, followed by the massive inputs of nutrients (e.g. P, Fe). D, the humidity decreased and massive mudstones were deposited after the volcanism in the Qinling orogenic belts. UV = ultraviolet light; S = stratosphere; T = troposphere; S-MIF = mass-independent fractionation of sulfur isotope.

in Fig. 1A). Based on the periods of localized volcanic activities in the western Tethys domain and the South China Plate, we speculate that the differences in the environmental perturbation and carbon isotope disturbance between these two regions are related to the localized volcanic activities during the CPE interval. In the western Tethys domain (Fig. 8A), during the Carnian age, the CO_2 released from the W-LIP eruption was conductive to the sudden changes of the carbonate factory on platforms after 234 Ma, i.e. from high-relief carbonate platforms to metazoan carbonate platforms (Fig. 8A). In addition to the W-LIP, there were still multistage volcanic activities in the western Tethys domain (Fig. 8A). These volcanic activities generally occurred during each period of negative $\delta^{13}C_{org}$ excursion and siliciclastic deposition from 234 Ma to 230.6 Ma (Fig. 8A). It suggests that frequent localized volcanic activities may complicate the environmental evolution in the western Tethys domain, further inducing multistage NCIEs and siliciclastic depositions. In the South China, during the Carnian age, volcanic activities generally occurred in the relatively concentrated periods before 234 Ma (Fig. 8B). From 234 Ma to 230.6 Ma, frequent localized volcanic activities were relatively weak in the process of environmental perturbation caused by the W-LIP eruption. It finally resulted in only one stage of environmental perturbation from 234 Ma to 230.6 Ma, such as the increases in temperature and reducibility, followed by the stable siliciclastic deposition in South China Plate (Fig. 8B). Therefore, during the CPE interval, the influence of localized volcanic activities around the world on environmental perturbation is nontrivial. These volcanic activities may further regulate the environmental evolution during the CPE interval in each local area, thereby causing the significant differences in environmental perturbations among different regions.

6. Conclusions

During the Carnian age of the Late Triassic, the Ordos Basin on the North China Plate experienced frequent environmental perturbation, including four humid episodes, four stages of temperature and lake-level rise, and four stages of NCIEs. This environmental perturbation occurred during the CPE interval and induced the synchronous sedimentary change, i.e. transition from massive mudstones to organic-rich shales.

Multistage volcanic activities in the Qinling orogenic belts proved to be the key factor for inducing the humid episodes, as well as temperature and lake-level rises in the Ordos Basin during the CPE interval. The emission of volcanic CO_2 from the Qinling orogenic belts synchronously induced the multiple NCIEs during the period of environmental perturbation. Additionally, the produced pyroclastic deposits in the Qinling orogenic belts entered the Ordos Basin, altering the provenance of sediments and providing the nutrients (e.g. P, Fe). The input of these nutrients stimulated the bloom of heat- and acid-resistant algae in the period of increased reducibility of the water column, resulting in the increased organic carbon burial. The provenance changes and organic-matter enrichment finally promoted the transition from massive mudstones to organic-rich shales in the Ordos Basin.

Globally, during the period of global climate perturbation driven by the W-LIP eruption, localized volcanic activities contributed significantly to the environment perturbation and induced higher-frequent environmental perturbation during the CPE interval. The frequent short-term localized volcanic activities complicated the environmental evolution during the CPE interval, resulting in the occurrences of multistage short-lived NCIEs and multiple extreme-humid episodes during the CPE interval. However, in the regions lacking localized volcanic activities, the W-LIP eruption dominated the environmental perturbation, resulting in the long-lasting NCIE and the stable humid

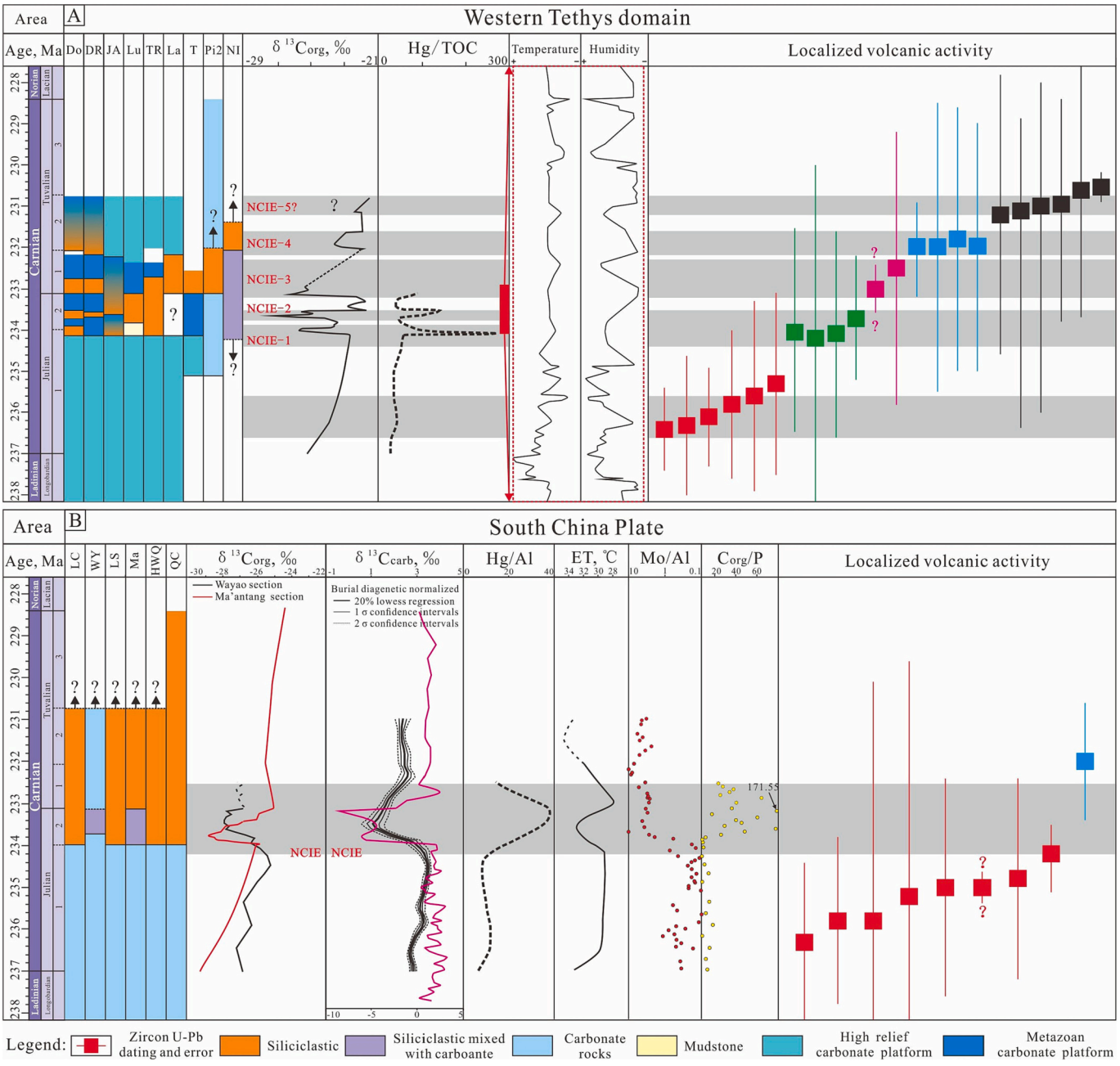

Fig. 8. Sedimentary changes, NCIEs and paleoenvrionmental perturbations in the T and SC areas in Fig. 1A. A, western Tethys domain (T area in Fig. 1A). Do = Dolomites section (Dal Corso et al., 2018); DR = Drau Range (Dal Corso et al., 2018); JA = Julian Alps (Dal Corso et al., 2018); Lu = Lunz (Mueller et al., 2016); TR = Transdanubian Range (Dal Corso et al., 2018; Baranyi et al., 2019); La = Lagonegro (Rigo et al., 2007; Dal Corso et al., 2018); T = Turkey (Lukeneder et al., 2012); Pi2 = Pignola 2 (Rigo et al., 2007); NI = North Italy (Meng et al., 2021); $\delta^{13}C_{org}$, Hg/TOC are modified from Dal Corso et al. (2018) and Mazaheri-Johari et al. (2021); perturbations of temperature and humidity are modified from Mueller et al. (2016); volcanic activities include the white number 12 to 16 in Fig. 1 and the U—Pb dating of the volcanism are listed in Table S2. In the study of the Dolomites section, the high-relief platforms were essentially built by microbial carbonate factories, while the metazoan carbonate platforms were built by the metazoan factory (Dal Corso et al., 2015). The shifts from high-relief carbonate platforms to metazoan carbonate platforms marks the crisis of the microbial factories after 234 Ma. B, South China (SC area in Fig. 1A); LC = Longchang section (Sun et al., 2016); WY = Wayao section (Zhao et al., 2022); LS = Laishike section (Zhao et al., 2022); Ma = Ma'antang section (Shi et al., 2019); HWQ = HWQ section (Li et al., 2020); QC = Quemo CO section (Fu et al., 2020); $\delta^{13}C_{org}$ from different sections are modified from Zhao et al. (2022), Sun et al. (2016), and Shi et al. (2019), respectively; the black curve of $\delta^{13}C_{carb}$ after diagenetic normalized are synthesized by the data from HWG, HWQ, Yongyue and Longchang sections from South China (Li et al., 2020); the pink curve of $\delta^{13}C_{carb}$ is from Qinghai-Tibet Plateau (modified from Fu et al. (2020)); Hg/Al, Mo/Al and C_{org}/P are modified from Zhao et al. (2022); ET = estimated temperature (Sun et al., 2016); volcanic activities include the white number 26 to 28 in Fig. 1 and the U—Pb dating of the volcanism are listed in Table S2. The dotted lines in B indicate the time corresponding to the top of the curves are uncertain. (For interpretation of the references to colour in this figure legend, the reader is referred to the web version of this article.)

episode during the CPE interval.

CRediT authorship contribution statement

Miruo Lin: Conceptualization, Investigation, Methodology, Writing – original draft. **Kelai Xi:** Investigation, Writing – review & editing. **Yingchang Cao:** Investigation, Writing – review & editing. **Xiaobing Niu:** Investigation. **Weijiao Ma:** Investigation. **Xiujuan Wang:** Investigation. **Shang Xu:** Investigation.

Declaration of competing interest

The authors declare that they have no known competing financial interests or personal relationships that could have appeared to influence the work reported in this paper.

Data availability

Data will be made available on request.

Acknowledgements

This study was co-supported by Innovation Research Group of the National Science Foundation (Grant No. 41821002), the National Natural Science Foundation of China (Grant No. 42072161), Fundamental Research Funds for the Central Universities (Grant No. 22CX07008A) and Taishan Scholars Program (tsqn202306125). We would like to thank the Changqing Oilfield Company of PetroChina for providing the relevant core samples and geological data of the Chang 7_3 sub-member, Ordos Basin.

Appendix A. Supplementary data

Supplementary data to this article can be found online at https://doi.org/10.1016/j.palaeo.2024.112012.

References

Andrusevich, V.E., Engel, M.H., Zumberge, J.E., Brothers, L.A., 1998. Secular, episodic changes in stable carbon isotope composition of crude oils. Chem. Geol. 152, 59–72.
Baranyi, V., Miller, C.S., Ruffell, A., Hounslow, M.W., Kürschner, W.M., 2019. A continental record of the Carnian Pluvial Episode (CPE) from the Mercia Mudstone Group (UK): palynology and climatic implications. J. Geol. Soc. London 176 (1), 149–166.
Baroni, M., Thiemens, M.H., Delmas, R.J., Savariano, J., 2007. Mass-independent sulfur isotopic compositions in stratospheric volcanic eruption. Science 315, 84–87.
Bernardi, M., Gianolla, P., Petti, F.M., Mietto, P., Benton, M.J., 2018. Dinosaur diversification linked with the Carnian Pluvial Episode. Nat. Commun. 9 (1), 1–10.
Berner, R.A., 1997. The rise of plants and their effect on weathering and atmospheric CO_2. Science 276 (5312), 544–546.
Blum, J.D., Sherman, L.S., Johnson, M.W., 2014. Mercury isotopes in earth and environmental sciences. Annu. Rev. Earth Planet. Sci. 42, 249–269.
Brucker, R.P., McManus, J., Severmann, S., Owens, J., Lyons, T.W., 2011. Trace metal enrichments in Lake Tanganyika sediments: controls on trace metal burial in lacustrine systems. Geochim. Cosmochim. Acta 75 (2), 483–499.
Carapezza, M.L., Barberi, F., Ranaldi, M., Ricci, T., Tarchini, L., Barrancos, J., Fischer, C., Perez, N., Weber, K., Di Piazza, A., Gattuso, A., 2011. J. Volcanol. Geotherm. Res. 207, 103–144.
Carrillo, U., Díaz-Villanueva, V., 2021. Impacts of volcanic eruptions and early recovery in freshwater environments and organisms. Biol. Rev. 96 (6), 2546–2560.
Chen, P., Xian, B., Li, M., Fang, L., Rahman, N.U., Liu, J., Chen, S., Tian, R., Wu, Q., 2023. Intensified lacustrine turbidite deposition as a response to the Carnian Pluvial Episode: insights from the Triassic Ordos Basin in North China Plate. Palaeogeogr. Palaeoclimatol. Palaeoecol. 623, 111599.
Colombi, C.E., Limarino, C.O., Alcober, O.A., 2017. Allogenic controls on the fluvial architecture and fossil preservation of the Upper Triassic Ischigualasto Formation, NW Argentina. Sediment. Geol. 362, 1–16.
Colombi, C., Martínez, R.N., Césari, S.N., Alcober, O., Limarino, C.O., Montañez, I., 2021. A high-precision U-Pb zircon age constraints the timing of the faunistic and palynofloristic events of the Carnian Ischigualasto Formation, San Juan, Argentina. J. South Am. Earth Sci. 111, 103433.
Dal Corso, J., Gianolla, P., Newton, R.J., Franceschi, M., Roghi, G., Caggiati, M., Raucsik, B., Budai, T., Hass, J., Preto, N., 2015. Carbon isotope records reveal synchronicity between carbon cycle perturbation and the "Carnian Pluvial Event" in the Tethys realm (Late Triassic). Global Planet. Change 127, 79–90.
Dal Corso, J., Ruffell, A., Preto, N., 2018. The Carnian pluvial episode (Late Triassic): new insights into this important time of global environmental and biological change. J. Geol. Soc. London 175 (6), 986–988.
Dal Corso, J., Bernardi, M., Sun, Y., Song, H., Seyfullah, L.J., Preto, N., Gianolla, P., Ruffell, A., Kustatscher, E., Roghi, G., Merico, A., Hohn, S., Shmidt, A.R., Marzoli, A., Newton, R., Wignall, P.B., Benton, M.J., 2020. Extinction and dawn of the modern world in the Carnian (Late Triassic). Sci. Adv. 6 (38), eaba0099.
Dal Corso, J., Mills, B.J., Chu, D., Newton, R.J., Song, H., 2022. Background Earth system state amplified Carnian (Late Triassic) environmental changes. Earth Planet. Sci. Lett. 578, 117321.
Fike, D.A., Bradley, A.S., Rose, C.V., 2015. Rethinking the ancient sulfur cycle. Annu. Rev. Earth Planet. Sci. 43, 593–622.
Fu, J.H., Li, S.X., Xu, L.M., Niu, X.B., 2018. Paleo-sedimentary environmental restoration and its significance of Chang 7 Member of Triassic Yanchang Formation in Ordos Basin, NW China. Petrol. Explorat. Dev. 45 (6), 998–1008.
Fu, X., Wang, J., Wen, H., Wang, Z., Zeng, S., Song, C., Chen, W.B., Wan, Y., 2020. A possible link between the Carnian Pluvial Event, global carbon-cycle perturbation, and volcanism: new data from the Qinghai-Tibet Plateau. Global Planet. Change 194, 103300.
Furin, S., Preto, N., Rigo, M., Roghi, G., Gianolla, P., Crowley, J.L., Bowring, S.A., 2006. High-precision U-Pb zircon age from the Triassic of Italy: implications for the Triassic time scale and the Carnian origin of calcareous nannoplankton and dinosaurs. Geology 34 (12), 1009–1012.
Grasby, S.E., Shen, W., Yin, R., Gleason, J.D., Blum, J.D., Lepak, R.F., Hurley, J.P., Beauchamp, B., 2017. Isotopic signatures of mercury contamination in latest Permian oceans. Geology 45 (1), 55–58.
Guex, J., Bartolini, A., Atudorei, V., Taylor, D., 2004. High-resolution ammonite and carbon isotope stratigraphy across the Triassic–Jurassic boundary at New York Canyon (Nevada). Earth Planet. Sci. Lett. 225 (1–2), 29–41.
Hayashi, K.I., Fujisawa, H., Holland, H.D., Ohmoto, H., 1997. Geochemistry of ~1.9 Ga sedimentary rocks from northeastern Labrador, Canada. Geochim. Cosmochim. Acta 61 (19), 4115–4137.
Hernández, P.A., Notsu, K., Salazar, J.M., Mori, T., Natale, G., Okada, H., Virgili, G., Shimoike, Y., Sato, M., Pérez, N.M., 2001a. Carbon dioxide degassing by advective flow from Usu Volcano, Japan. Science 292, 5514.
Hernández, P.A., Salazar, J.M., Shimoike, Y., Mori, T., Notsu, K., Pérez, N., 2001b. Diffuse emission of CO2 from Miyakejima volcano, Japan. Chem. Geol. 177, 175–185.
Hintelmann, H., Lu, S., 2003. High precision isotope ratio measurements of mercury isotopes in cinnabar ores using multi-collector inductively coupled plasma mass spectrometry. Analyst 128 (6), 635–639.
Hornung, T., Krystyn, L., Brandner, R., 2007. A Tethys-wide mid-Carnian (Upper Triassic) carbonate productivity crisis: evidence for the Alpine Reingraben event from Spiti (Indian Himalaya)? J. Asian Earth Sci. 30 (2), 285–302.
Jiang, Y.H., Jin, G.D., Liao, S.Y., Zhou, Q., Zhao, P., 2010. Geochemical and Sr-Nd-Hf isotopic constraints on the origin of Late Triassic granitoids from the Qinling orogen, central China: implications for a continental arc to continent–continent collision. Lithos 117, 183–197.
Jin, X., Baranyi, V., Caggiati, M., Franceschi, M., Wall, C.J., Liu, G.L., Schmitz, M.D., Gianolla, P., Ogg, J.G., Lu, G., Shi, Z.Q., Preto, N., 2021. Middle Triassic lake deepening in the Ordos Basin of North China linked with global sea-level rise. Global Planet. Change 207, 103670.
Kiessling, W., 2010. Reef expansion during the Triassic: spread of photosymbiosis balancing climatic cooling. Palaeogeogr. Palaeoclimatol. Palaeoecol. 290 (1–4), 11–19.
Korte, C., Kozur, H.W., 2010. Carbon-isotope stratigraphy across the Permian–Triassic boundary: a review. J. Asian Earth Sci. 39 (4), 215–235.
Li, Z.C., Zhang, X.K., Zeng, J.J., Qi, J.H., Zhang, H.F., Yang, Z.Y., 2019. The characteristics and geological significance of the Adakite rocks of the upper Triassic stata Huari formation volcanics in west Qinling. Miner. Explorat. 10 (6), 1361–1368.
Li, Z., Chen, Z.Q., Zhang, F., Ogg, J.G., Zhao, L., 2020. Global carbon cycle perturbations triggered by volatile volcanism and ecosystem responses during the Carnian Pluvial Episode (late Triassic). Earth-Sci. Rev. 211, 103404.
Liu, B.C., Li, K.N., Shi, H.L., Pu, W.F., Wang, H.T., Wang, S.H., 2018. Petrogenesis and tectonic implications of late Triassic volcanic rocks at the Gansu-Qinghai junction in the west Qinling mountains. Geoscience 32 (4), 704–717.
Liu, X., Li, S., Guo, Q., Zhou, X., Liu, J., 2021. Characteristics of rock types and exploration significance of the shale strata in the Chang 7_3 sub-member of Yanchang Formation, Ordos Basin, China. J. Nat. Gas Geosci. 6 (6), 363–373.
Lloyd, R.M., 1964. Variations in the oxygen and carbon isotope ratios of Florida Bay mollusks and their environmental significance. J. Geol. 72, 84–111.
Lu, J., Zhang, P., Dal Corso, J., Yang, M., Wignall, P.B., Greene, S.E., Shao, L.Y., Lyu, D., Hilton, J., 2021. Volcanically driven lacustrine ecosystem changes during the Carnian Pluvial Episode (Late Triassic). Proc. Natl. Acad. Sci. 118 (40), e2109895118.
Lukeneder, S., Lukeneder, A., Harzhauser, M., İslamoğlu, Y., Krystyn, L., Lein, R., 2012. A delayed carbonate factory breakdown during the Tethyan-wide Carnian Pluvial Episode along the Cimmerian terranes (Taurus, Turkey). Facies 58 (2), 279–296.
Martín-Puertas, C., Valero-Garcés, B.L., Mata, M.P., Moreno, A., Giralt, S., Martínez-Ruiz, F., Jiménez-Espejo, F., 2011. Geochemical processes in a Mediterranean Lake: a high-resolution study of the last 4,000 years in Zonar Lake, southern Spain. J. Paleolimnol. 46 (3), 405–421.

Mazaheri-Johari, M., Gianolla, P., Mather, T.A., Frieling, J., Chu, D., Dal Corso, J., 2021. Mercury deposition in Western Tethys during the Carnian Pluvial Episode (Late Triassic). Sci. Rep. 11 (1), 1–10.
Mchone, J.G., 2003. Volatile emissions from Central Atlantic Magmatic Province basalts: mass assumptions and environmental consequences. Geophys. Monogr. Am. Geophys. Union 136, 241–254.
Meixnerová, J., Blum, J.D., Johnson, M.W., Stüeken, E.E., Kipp, M.A., Anbar, A.D., Buick, R., 2021. Mercury abundance and isotopic composition indicate subaerial volcanism prior to the end-Archean "whiff" of oxygen. Proc. Natl. Acad. Sci. 118 (33), e2107511118.
Meng, Z., Wang, J.G., Garzanti, E., Han, Z., Chen, G., 2021. Late Triassic rifting and volcanism on the northeastern Indian margin: a new phase of Neo-Tethyan seafloor spreading and its paleogeographic implications. Palaeogeogr. Palaeoclimatol. Palaeoecol. 570, 110367.
Meyers, P.A., 1994. Preservation of elemental and isotopic source identification of sedimentary organic matter. Chem. Geol. 114, 289–302.
Mueller, S., Krystyn, L., Kürschner, W.M., 2016. Climate variability during the Carnian Pluvial Phase-a quantitative palynological study of the Carnian sedimentary succession at Lunz am See, Northern Calcareous Alps, Austria. Palaeogeogr. Palaeoclimatol. Palaeoecol. 441, 198–211.
Niem, A.R., 1977. Mississippian pyroclastic flow and ash-fall deposits in the deep-marine Ouachita flysch basin, Oklahoma and Arkansas. Geol. Soc. Am. Bull. 88 (1), 49–61.
Ohmoto, H., 2020. A seawater-sulfate origin for early Earth's volcanic sulfur. Nat. Geosci. 13 (8), 576–583.
Panchuk, K.M., Holmden, C.E., Leslie, S.A., 2006. Local controls on carbon cycling in the Ordovician midcontinent region of North America, with implications for carbon isotope secular curves. J. Sediment. Res. 76 (2), 200–211.
Patterson, W.P., Walter, L.M., 1994. Depletion of 13C in seawater ΣCO_2 on modern carbonate platforms: significance for the carbon isotopic record of carbonates. Geology 22 (10), 885–888.
Peng, J., Slater, S.M., Vajda, V., 2022. A Late Triassic vegetation record from the Huangshanjie Formation, Junggar Basin, China: possible evidence for the Carnian Pluvial Episode. Geol. Soc. Lond. Spec. Publ. 521 (1), 95–108.
Percival, L.M., Ruhl, M., Hesselbo, S.P., Jenkyns, H.C., Mather, T.A., Whiteside, J.H., 2017. Mercury evidence for pulsed volcanism during the end-Triassic mass extinction. Proc. Natl. Acad. Sci. 114 (30), 7929–7934.
Philippot, P., Van Zuilen, M., Rollion-Bard, C., 2012. Variations in atmospheric sulphur chemistry on early Earth linked to volcanic activity. Nat. Geosci. 5 (9), 668–674.
Preto, N., Kustatscher, E., Wignall, P.B., 2010. Triassic climates-state of the art and perspectives. Palaeogeogr. Palaeoclimatol. Palaeoecol. 290 (1–4), 1–10.
Qin, J.F., Lai, S.C., Li, Y.F., 2013. Multi-stage granitic magmatism during exhumation of subducted continental lithosphere: Evidence from the Wulong pluton, South Qinling. Gondwana Res. 24, 1108–1126.
Qiu, X., Liu, C., Mao, G., Deng, Y., Wang, F., Wang, J., 2014. Late Triassic tuff intervals in the Ordos basin, Central China: their depositional, petrographic, geochemical characteristics and regional implications. J. Asian Earth Sci. 80, 148–160.
Qiu, X.W., Liu, C.Y., Mao, G.Z., Deng, Y., Wang, F.F., Wang, J.Q., 2015. Major, trace and platinum-group element geochemistry of the Upper Triassic nonmarine hot shales in the Ordos basin, Central China. Appl. Geochem. 53, 42–52.
Rigo, M., Preto, N., Roghi, G., Tateo, F., Mietto, P., 2007. A rise in the carbonate compensation depth of western Tethys in the Carnian (Late Triassic): deep-water evidence for the Carnian Pluvial Event. Palaeogeogr. Palaeoclimatol. Palaeoecol. 246 (2–4), 188–205.
Roijackers, R.M.M., Kessels, H., 1986. Ecological characteristics of scale-bearing Chrysophyceae from The Netherlands. Nord. J. Bot. 6 (3), 373–385.
Ruffell, A., Simms, M.J., Wignall, P.B., 2016. The Carnian Humid Episode of the late Triassic: a review. Geol. Mag. 153 (2), 271–284.
Sanei, H., Grasby, S.E., Beauchamp, B., 2012. Latest Permian mercury anomalies. Geology 40 (1), 63–66.
Scotese, C.R., 2014. Atlas of Permo-Triassic Paleogeographic Maps (Mollweide Projection), Maps 43–52, Volumes 3 & 4 of the PALEOMAP Atlas for ArcGIS. PALEOMAP Project, Evanston, IL.
Shen, Y., Farquhar, J., Zhang, H., Masterson, A., Zhang, T., Wing, B.A., 2011. Multiple S-isotopic evidence for episodic shoaling of anoxic water during Late Permian mass extinction. Nat. Commun. 2, 210.
Shi, Z., Jin, X., Preto, N., Rigo, M., Du, Y., Han, L., 2019. The Carnian Pluvial Episode at Ma'antang, Jiangyou in Upper Yangtze Block, Southwestern China. J. Geol. Soc. London 176 (1), 197–207.
Shukla, U.K., Bachmann, G.H., Singh, I.B., 2010. Facies architecture of the Stuttgart Formation (Schilfsandstein, Upper Triassic), central Germany, and its comparison with modern Ganga system, India. Palaeogeogr. Palaeoclimatol. Palaeoecol. 297 (1), 110–128.
Simms, M.J., Ruffell, A.H., 1989. Synchroneity of climatic change and extinctions in the late Triassic. Geology 17 (3), 265–268.
Stanley, D.J., 1983. Parallel laminated deep-sea muds and coupled gravity flow-hemipelagic settling in the Mediterranean. Smithson. Contrib. Mar. Sci. 19, 1–17.
Sun, Y.D., Wignall, P.B., Joachimski, M.M., Bond, D.P., Grasby, S.E., Lai, X.L., Wang, L. N., Zhang, Z.T., Sun, S., 2016. Climate warming, euxinia and carbon isotope perturbations during the Carnian (Triassic) Crisis in South China. Earth Planet. Sci. Lett. 444, 88–100.
Sun, Y.D., Richoz, S., Krystyn, L., Zhang, Z.T., Joachimski, M.M., 2019. Perturbations in the carbon cycle during the Carnian Humid Episode: carbonate carbon isotope records from southwestern China and northern Oman. J. Geol. Soc. London 176 (1), 167–177.
Sun, Y., Li, X., Liu, Q., Zhang, M., Li, P., Zhang, R., Shi, X., 2020. In search of the inland carnian pluvial event: middle–upper triassic transition profile and U–Pb isotopic dating in the Yanchang Formation in Ordos Basin, China. Geol. J. 55, 4905–4919.
Tasić, M.B., Pinto, L.F.R., Klein, B.C., Veljković, V.B., Maciel Filho, R., 2016. *Botryococcus braunii* for biodiesel production. Renew. Sustain. Energy Rev. 64, 260–270.
Them II, T.R., Jagoe, C.H., Caruthers, A.H., Gill, B.C., Grasby, S.E., Gröcke, D.R., Yin, R., Owens, J.D., 2019. Terrestrial sources as the primary delivery mechanism of mercury to the oceans across the Toarcian Oceanic Anoxic Event (Early Jurassic). Earth Planet. Sci. Lett. 507, 62–72.
Thibodeau, A.M., Ritterbush, K., Yager, J.A., West, A.J., Ibarra, Y., Bottjer, D.J., Berelson, W.M., Bergquist, B.A., Corsetti, F.A., 2016. Mercury anomalies and the timing of biotic recovery following the end-Triassic mass extinction. Nat. Commun. 7 (1), 1–8.
Trotter, J.A., Williams, I.S., Nicora, A., Mazza, M., Rigo, M., 2015. Long-term cycles of Triassic climate change: a new δ18O record from conodont apatite. Earth Planet. Sci. Lett. 415, 165–174.
Wang, R.G., Li, W.H., Liao, Y.Y., Guo, Y.Q., Liu, H.W., 2013. Provenance analysis of Chang 7 Member of Triassic Yanchang Formation in Ordos Basin. Geol. Bull. China 32 (4), 671–684.
Wang, X., Cawood, P.A., Zhao, H., Zhao, L., Grasby, S.E., Chen, Z.Q., Wignall, P.B., Lv, Z. Y., Han, C., 2018. Mercury anomalies across the end Permian mass extinction in South China from shallow and deep water depositional environments. Earth Planet. Sci. Lett. 496, 159–167.
Wignall, P.B., 2001. Large igneous provinces and mass extinctions. Earth Sci. Rev. 53 (1–2), 1–33.
Xi, K.L., Cao, Y.C., Lin, M.R., Liu, K.Y., Wu, S.T., Yuan, G.H., Yang, T., 2019. Applications of light stable isotopes (C, O, H) in the study of sandstone diagenesis: a review. Acta Geol. Sin. Engl. Edn. 93 (1), 213–226.
Xi, K.L., Li, K., Cao, Y.C., Lin, M.R., Niu, X.B., Zhu, R.K., Wei, X.Z., You, Y., Liang, X.W., Feng, S.B., 2020. Laminae combination and shale oil enrichment patterns of Chang 7_3 sub-member organic-rich shales in the Triassic Yanchang Formation, Ordos Basin, NW China. Petrol. Explorat. Dev. 47 (6), 1342–1353.
Zambardi, T., Sonke, J.E., Toutain, J.P., Sortino, F., Shinohara, H., 2009. Mercury emissions and stable isotopic compositions at Vulcano Island (Italy). Earth Planet. Sci. Lett. 277 (1–2), 236–243.
Zhang, W.Z., Yang, H., Xia, X.Y., Xie, L.Q., Xie, G.W., 2016. Triassic chrysophyte cyst fossils discovered in the Ordos Basin, China. Geology 44 (12), 1031–1034.
Zhang, W., Yang, W., Xie, L., 2017. Controls on organic matter accumulation in the Triassic Chang 7 lacustrine shale of the Ordos Basin, central China. Int. J. Coal Geol. 183, 38–51.
Zhang, K., Liu, R., Liu, Z.J., Li, L., 2021a. Geochemical characteristics and geological significance of humid climate events in the Middle-Late Triassic (Ladinian-Carnian) of the Ordos Basin, central China. Mar. Pet. Geol. 131, 105179.
Zhang, B., Mao, Z.G., Zhang, Z.Y., Yuan, Y.L., Chen, X.L., Shi, Y.X., Liu, G.L., Shao, X.Z., 2021b. Black shale formation environment and its control on shale oil enrichment in Triassic Chang 7 Member, Ordos Basin, NW China. Petrol. Explorat. Dev. 48 (6), 1304–1314.
Zhao, H., Grasby, S.E., Wang, X., Zhang, L., Liu, Y., Chen, Z., Hu, Z., Huang, Y., 2022. Mercury enrichments during the Carnian Pluvial Event (Late Triassic) in South China. GSA Bull. 134 (9–10), 2709–2720.
Zhou, D.W., Zhao, C.Y., Li, Y.D., Jian, W.C., Ye, J., Chen, G., 1995. Geological features of southwest margin of Ordos basin and its relationships with Qinling orogenic belt. Geological Publishing House, Beijing.